RSC Advances

ROYAL SOCIETY
OF CHEMISTRY

REVIEW

View Article Online
View Journal | View Issue

Cite this: *RSC Adv.*, 2022, **12**, 29826

Molybdenum disulfide (MoS_2) based photoredox catalysis in chemical transformations

Praveen P. Singh,[a] Surabhi Sinha,[a] Geetika Pandey[b] and Vishal Srivastava*[c]

Received 9th September 2022
Accepted 11th October 2022

DOI: 10.1039/d2ra05695j

rsc.li/rsc-advances

Photoredox catalysis has been explored for chemical reactions by irradiation of photoactive catalysts with visible light, under mild and environmentally benign conditions. Furthermore, this methodology permits the activation of abundant chemicals into valuable products through novel mechanisms that are otherwise inaccessible. In this context, MoS_2 has drawn attention due to its excellent solar spectral response and its notable electrical, optical, mechanical and magnetic properties. MoS_2 has a number of characteristic properties like tunable band gap, enhanced absorption of visible light, a layered structure, efficient photon electron conversion, good photostability, non-toxic nature and quantum confinement effects that make it an ideal photocatalyst and co-catalyst for chemical transformations. Recently, MoS_2 has gained synthetic utility in chemical transformations. In this review, we will discuss MoS_2 properties, structure, synthesis techniques, and photochemistry along with modifications of MoS_2 to enhance its photocatalytic activity with a focus on its applications and future challenges.

1 Introduction

Molybdenum disulfide (MoS_2) is an inorganic compound of the transition metal dichalcogenide (TMD) series. It is one of the most used photocatalysts that has a wide range of applications in different fields. It is applicable to degrade pharmaceutically active compounds (PhACs), synthetic dyes (rhodamine B, methylene blue, methyl orange and novacron red Hunts-man), pesticides and herbicides. It also employed for photocatalytic evolution of oxygen, nitrogen fixation, ammonia synthesis and water electrolysis.[1–7]

In recent years, MoS_2 has received much attention due to its unique electrical and optical properties.[8a] MoS_2 is a two-dimensional (2D) transition metal dichalcogenide, a narrow band semiconductor with a band gap of 1.9 eV which can be altered by adjusting the number of layers. Among all 2D TMDs, MoS_2 is one of the few with a natural layered structure, indicating that MoS_2 can be stripped to obtain high-quality 2D MoS_2 without complicated chemical synthesis.[8b] Therefore, the cost of preparing 2D MoS_2 is much lower than other 2D TMDs due to

---

[a] *Department of Chemistry, United College of Engineering & Research, Prayagraj 211002, Uttar Pradesh, India. E-mail: ppsingh23@gmail.com*
[b] *Department of Physics, United University, Prayagraj 211012, Uttar Pradesh, India*
[c] *Department of Chemistry, CMP Degree College, University of Allahabad, Prayagraj-211002, Uttar Pradesh, India. E-mail: vishalgreenchem@gmail.com*

Praveen P. Singh is working as Assistant Professor in the Department of Chemistry at the United College of Engineering and Research, Prayagraj, India. He obtained his BSc, MSc degree in Organic Chemistry from T. D. P. G. College (V. B. S Purvanchal University) Jaunpur and DPhil from the Department of Chemistry, University of Allahabad, India. His current research interests include the development of synthetic receptors for the recognition of biological target structures and the application of visible light chemical photocatalysis towards organic synthesis as well as nanophotocatalysis.

Surabhi Sinha is presently working as an Assistant Professor in the Department of Chemistry, United College of Engineering & Research, Naini, Prayagraj. She has completed her graduation, post-graduation and DPhil from the University of Allahabad, Prayagraj. Her area of research interest mainly includes quaternary complexes of biochemical significance and organic synthetic transformations. She is a life member of several professional bodies.

the simple synthesis conditions. More importantly, 2D MoS_2 is a 2D semiconductor with a direct band-gap, which has the best electric performance among 2D TMDs.[8c] These make 2D MoS_2 get more attention among 2D TMDs.

Several characteristics of MoS_2 such as high absorbance in the visible region,[9] high carrier mobility,[10] stability,[11] preferable catalytic activity,[12] good photostability,[13] outstanding electrochemical properties,[14] strong surface adsorption capacity and higher specific surface area[15] favours its application as a photocatalyst as well as a co-catalyst and also, it is capable of addressing the limitations faced by typical photocatalysts. Additionally, MoS_2 is found to be abundant and cheap.[7] Currently, semiconductor photocatalysts with controllable morphologies are gaining significant attraction in applications associated with environmental remediation process.[16] Phase engineering, defect engineering, doping of external materials, interlayer engineering, surface modification, and heterojunction[17a,b] construction make MoS_2 more flexible in terms of tuning its properties during synthesis.

Molybdenum disulfide (MoS_2)[17c] has emerged as one of the most important two-dimensional functional materials, popular new co-catalysts due to their excellent photocatalytic activity, substantial adsorptivity, great value and its non-toxicity. The visible region of electromagnetic spectrum exhibits the absorption spectrum of 2D MoS_2, providing a plethora of opportunities for widespread applications.[17d] Applications for MoS_2-based materials are said to include energy storage,[17e] hydrogen production,[17f] pollutant degradation,[17g] disinfection,[17h] *etc.* Numerous studies have recently provided a summary of photocatalytic properties of MoS_2 for numerous application areas.[17i–n]

In continuation of our work on photocatalysed organic synthesis[18,19] this review aims to provide a comprehensive report on the current research, especially the role of MoS_2 in the chemical transformation.

2 Synthesis of MoS_2

For the most part, two different synthetic procedures are used to create MoS_2: (1) a top-down strategy that involves exfoliating bulk MoS_2 to create materials with one or two monolayers, and (2) a bottom-up strategy that uses techniques like hydrothermal or chemical vapour deposition. Several methods exist for the preparation of MoS_2 using different molybdenum precursors and sulfur sources, like elemental sulfur powder,[20] thiourea,[21] thioacetamide,[22] and L-cysteine.[23] By regulating variables such the reaction solvent, temperature, pH, reaction time, and the application of surfactants or ligands, which are essential for managing the synthesis to create the desired chalcogenide, a variety of fascinating morphologies can be created. Table 1 exhibits the different methods that have been used to synthesize MoS_2 materials alongside the applications of the synthesized materials. The most used methods are solid-state,[24] hydrothermal,[25,26] solvothermal,[27] and hybrid methods.[28,29]

The benefits and drawbacks of synthesis techniques[44] such as thermal annealing, plasma-assisted synthesis, magnetron sputtering-based synthesis, atomic layer deposition (ALD), and wet chemical processes are summarised in Fig. 1.

3 Properties of MoS_2

MoS_2 is a typical and stable 2D transition metal dichalcogenide which reveals that it is a semiconductor of MX_2 type where the transition metals denote M and the chalcogen denotes X[45] with three hexagonal planes (S–Mo–S), which is bonded to each other *via* ionic–covalent interactions.[46] The sandwiched MoS_2 is brought together to form sheets with an interlayer distance of 0.65 nm by the weak van der Waals force, which assumes responsibility for creating a 2D layered structure. Fig. 2a depicts the MoS_2 structure as described. In addition, Fig. 2b reflects the fact that the presence of impurities in MoS_2 alters its interlayer distance.[47] As an n-type semiconductor, MoS_2 has an indirect band gap of 1.2 eV in the bulk. The band gap of this semiconductor is inversely proportional to its number of layers. As a result, a direct band gap of 1.9 eV is obtained by almost reducing the number of layers to just one (Fig. 3c), making it a suitable photocatalyst in the visible region.[11] The narrow band gap facilitates its high absorption of light in the visible region.

Geetika Pandey is working as an Assistant Professor in the Department of Physics at the United University, Prayagraj, India. She obtained her BSc, MSc degree in Physics and DPhil from the Department of Physics, University of Allahabad, Prayagraj, India. Her current research interests include the condensed matter physics and photocatalysis of nanomaterials.

Vishal Srivastava is working as an Assistant Professor, Department of Chemistry, C.M.P. College, (Constituent P.G. College of Central University of Allahabad) Prayagraj, India. He has completed his graduation (BSc), post-graduation (MSc) in Organic Chemistry and Doctoral Degree (DPhil) from the Department of Chemistry, University of Allahabad, India. His current research work involves the designing of novel biologically active photoredox catalysed synthetic organic compounds.

Table 1 Synthesis Methods and Applications of MoS_2

No.	Synthesis method	Metal precursor used	Source of sulfur used	Morphology and particle size	Applications	Ref.
1	Colloidal	$Mo(CO)_6$	Sulfur powder	Nanosheets	Electrochemical studies	1
2	Hydrothermal	$(NH_4)Mo_7O_{24}\cdot 4H_2O$	Thiourea (H_2CSNH_2)	Layered MoS_2 nanoflowers with ~0.1 μm particle size	Photocatalytic degradation of methylene blue and crystal violet dyes	2
3	Hydrothermal	Sodium molybdate dihydrate ($Na_2MoO_4\cdot 2H_2O$)	Thioacetamide (C_2H_5NS)	Nano flowers with average size ~100 nm	Photocatalytic degradation of rhodamine B	3
4	Hydrothermal	Sodium molybdate dihydrate ($Na_2MoO_4\cdot 2H_2O$)	L-cysteine	Quantum dots with ~2.5 nm particle size	Detection of methyl parathion (pesticide)	4
5	Hydrothermal	$(NH_4)MoS_4$	$(NH_4)MoS_4$		Fluorescent probe for hyaluronidase detection	5
6	Chemical Exfoliation	Commercially available MoS_2 powder		Nanosheets	Photocatalytic oxidation of benzyl halides	6 30
7	Chemical vapor Deposition	Ammonium heptamolybdate	Sulfur	Not mentioned		7 31
8	Colloidal	Ammonium tetrathiomolybdate [$(NH_4)_2MoS_4$]	Ammonium tetrathiomolybdate [$(NH_4)_2MoS_4$]	Spherical quantum dots with average size ~5 nm	Bioimaging	8 32
9	Heating	$Mo(acac)_2$	1-Dodecanethiol	Nanosheet	Electrical bistability performance	9 33
10	Hot injection	Molybdenum(V) chloride ($MoCl_5$)	*N*,*N*′-diphenylthiourea	Nanosheets		10 34
11	Hydrothermal	Sodium molybdate dihydrate ($Na_2MoO_4\cdot 2H_2O$)	Thioacetamide (CH_3CSNH_2)	Coral-like	Lubrication additive; photocatalytic degradation of liquid paraffin	11 35
12	Hydrothermal	$Na_2MoO_4\cdot 2H_2O$	Cysteine	Quantum dots with 2 ~3.5 nm particle size	Fluorescent probe for sensing of hydroquinone and bioimaging	12 36
13	Solid state	$(NH_4)_6Mo_7O_{24}\cdot 4H_2O$	Sulfur	Nanosheets, thinner than 5 nm	Photocatalytic degradation of rhodamine B	24
14	Hydrothermal	$Na_2MoO_4\cdot 2H_2O$	Thiourea (H_2CSNH_2)	Irregular with average size in the range 12–25 nm	Electrochemical studies	25
15	Hydrothermal	Ammonium hepta molybdate tetrahydrate [$(NH_4)_6Mo_7O_{24}\cdot 4H_2O$]	Ammonium polysulfide	Ammonium polysulfide as the sulfur source: Uniform MoS_2 nanospheres with average size of ~100 nm	Lubrication additive	27
16	Hydrothermal	MoO_3	Potassium thiocyanate	Flowerlike MoS_2 spheres with average diameter of 1–2 nm	Photocatalytic degradation of methylene blue	37
17	Hydrothermal	$Na_2MoO_4\cdot 2H_2O$	L-cysteine	Microspheres comprising crossed-linked nanorods ~100 nm in length	Photocatalytic degradation of thiocarbamate herbicides	38
18	Hydrothermal	Ammonium tetrathiomolybdate [$(NH_4)_2MoS_4$]	Thiourea (H_2CSNH_2)	Flowerlike microsphere	Photocatalytic degradation of rhodamine B and methylene blue	39
19	Hydrothermal	$(NH_4)_6Mo_7O_{24}\cdot 4H_2O$	Thiourea	Nanosheets	Detection of dopamine	40
20	Hydrothermal	$(NH_4)_6Mo_7O_{24}\cdot 4H_2O$	Na_2S	Hierarchical porous with the thickness of ~20–40 nm	Detection of phenol sulphite oxidase, nicotinamide adenine dinucleotide oxidase and superoxide dismutase mimicking activities	41
21	Microwave	Ammonium tetrathiomolybdate [$(NH_4)_2MoS_4$]	Ammonium tetrathiomolybdate [$(NH_4)_2MoS_4$]	Quantum dots with average diameter of ~1.72 nm	Determination of terramycin	42
22	Solid state	$(NH_4)_2MoS_4$	Thiourea	Sheetlike structure and ultrathin layers	Electrochemical measurement	43

Crystal lattices of MoS_2 exists in four polymorphic forms namely 1H, 2H, 1T and 3R (H- Hexagonal, T-Tetragonal and R-Rhombohedral) which are classified based on the stacking arrangement and the co- ordination between Mo and S atoms (Fig. 2d).[11] MoS_2 is synthesized in various morphologies (Fig. 2e) which includes nanoflowers (Fig. 2e$_1$, Fig. 2e$_2$),[48] nanosheets (Fig. 2e$_3$, Fig. 2e$_4$),[49] nanoflakes,[50] nanocrystals, nanospheres,[51] nanoribbons,[52] nanotubes (Fig. 2e$_5$),[53] nanoworms (Fig. 2e$_6$),[54]

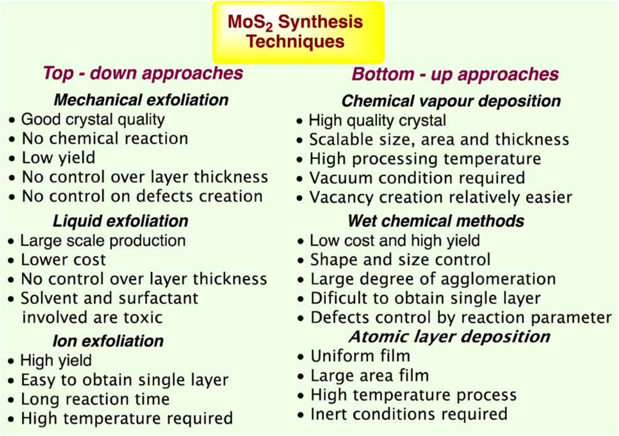

MoS_2 Synthesis Techniques

Top - down approaches

Mechanical exfoliation
- Good crystal quality
- No chemical reaction
- Low yield
- No control over layer thickness
- No control on defects creation

Liquid exfoliation
- Large scale production
- Lower cost
- No control over layer thickness
- Solvent and surfactant involved are toxic

Ion exfoliation
- High yield
- Easy to obtain single layer
- Long reaction time
- High temperature required

Bottom - up approaches

Chemical vapour deposition
- High quality crystal
- Scalable size, area and thickness
- High processing temperature
- Vacuum condition required
- Vacancy creation relatively easier

Wet chemical methods
- Low cost and high yield
- Shape and size control
- Large degree of agglomeration
- Dificult to obtain single layer
- Defects control by reaction parameter

Atomic layer deposition
- Uniform film
- Large area film
- High temperature process
- Inert conditions required

Fig. 1 MoS_2 synthesis techniques with their advantages and disadvantages.[44]

coral-like structures (Fig. 2e$_7$),[49] nanodots and quantum dots (Fig. 2e$_8$).[55]

Due to the 2D nature of MoS_2, it's intrinsic properties are greatly influenced by the surrounding environment on the nanoscale. The suspended structures in these systems are hybrid systems with transport performance,[56a–g] tunable optoelectronic behaviour,[56h–l] and nanomechanical properties,[56m–p] all of which are fascinating on their own. The size, surface area, and surface energy of the MoS_2 particles are determined by its morphology, which has a significant impact on how it executes in photocatalytic applications. Due to their large surface area and narrow band gap, MoS_2 nanoflowers are more effective for absorbtion of visible light, which improves their photocatalytic efficacy. The shape of MoS_2 nanoflowers determines their surface area, which in turn determines how well they operate as photocatalysts. MoS_2 is anisotropic, piezocatalytic,[56] hydrophobic and low-toxic, which has high specific surface area with high surface energy,[57] high surface to volume ratio, high e^- mobility, high optical absorption, high catalytic activity, good tribological properties,[58] good thermal stability and free sulfur groups.[59] Due to its low price and a wealth of earth reserves, it is commercially viable. As a result, MoS_2's characteristics are largely in favour of its application as a photocatalyst.

Unfortunately, the catalytic activity of MoS_2 is greatly inhibited due to its low dispersion ability which can be attributed to its hydrophobicity and low electrical conductivity.[60] The formation of composites using MoS_2 may be a viable and efficient way to get around this problem and maximise the benefits of MoS_2 as a photocatalyst in aqueous bodies because the

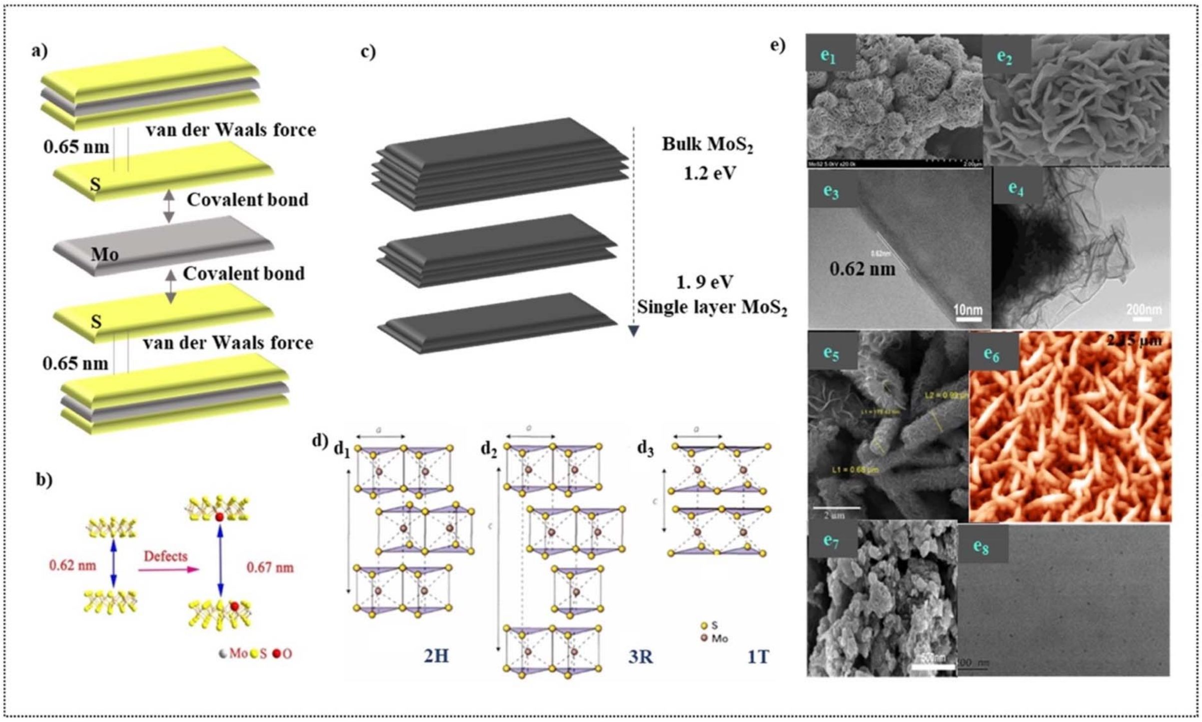

Fig. 2 (a). Visualization of the layered structure of MoS_2 and the forces responsible for its layered structure. (b). Pictorial illustration of the increased interlayer distance due to the presence of impurities. Adapted with permission from ref. 47, Copyrights 2022 Elsevier. (c). Graphical illustration of the tunable band gap exhibited by MoS_2. (d). Crystal structures of MoS_2. (d$_1$). 2H, (d$_2$). 3R and (d$_3$).1T. Adapted with permission from ref. 11, Copyrights 2022 Elsevier. (e). Different morphologies portrayed by MoS_2 (through synthesis) (e$_1$). Nanoflowers at the resolution of 2 μm (e$_2$). Nanoflowers at the resolution of 500 nm Adapted with permission from ref. 48, Copyrights 2022 Elsevier (e$_3$). TEM image of the nanosheets at 10 nm (e$_4$). TEM image of the nanosheets at 200 nm Adapted with permission from ref. 49, Copyrights 2022 Elsevier (e$_5$). Nanotubes Adapted with permission from ref. 53, Copyrights 2022 Elsevier (e$_6$). Nanoworms. Adapted with permission from ref. 54, Copyrights 2022 Elsevier (e$_7$). Coral-like structure. Adapted with permission from ref. 49 Copyrights 2022 Elsevier (e$_8$). Quantum dots. Reproduced from ref. 55 with permission from [Elsevier], Copyright [2022].

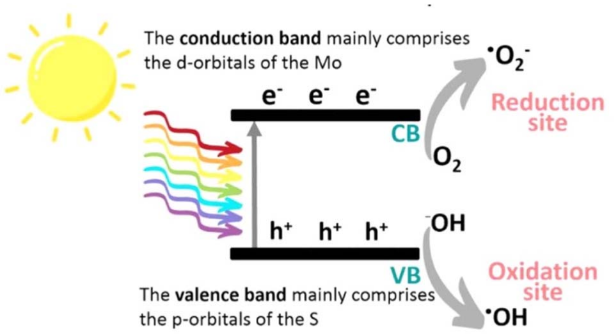

Fig. 3 Schematic illustration of the photocatalytic mechanism of MoS_2. Reproduced from ref. 29 with permission from [American Chemical Society], copyright [2022].

properties of other compounds in the composite may enhance the electrical conductivity and dispersion of MoS_2 and thereby facilitate the exhibition of its full potential and surplus advantages.

4 Photochemistry of MoS_2

MoS_2 has attracted significant attention, and a wide range of desirable photocatalytic properties have been reported, such as narrow band gap energy, excellent optical absorptivity, and high mobility of charge carriers, in addition to low toxicity and cost. However, the performance of MoS_2 is limited by photogenerated e^-/h^+ recombination, the edge activity effect, and photocorrosion. Past efforts to enhance the photocatalytic properties of MoS_2 have involved controlling the morphology, modulation of energy bands through doping, band alignment through heterojunction formation, modification with carbon nanostructures, and combining with metal particles exhibiting surface plasmon resonance.

The photocatalytic redox processes begin with the production of photoexcited charge carrier pairs (e^-/h^+). As illustrated in Fig. 3, upon irradiation the MoS_2 simultaneously generates e^- and h^+, where the photogenerated e^- is promoted to the CB, leaving behind the hole (h^+) in the VB. Subsequently, these photogenerated carriers migrate to the surface of the MoS_2 to participate in reduction (e^-) and oxidation (h^+) processes. Photoexcited e^- may react with adsorbed O_2 to produce $^{\bullet}O_2^-$ radicals and, simultaneously, the h^+ remaining in the VB can abstract an e^- from hydroxyl ions or adsorbed H_2O molecules to produce $^{\bullet}OH$ radicals, which are powerful oxidizing agents that can react with harmful organic, inorganic, and biological compounds.

5 Modifications of MoS_2 to improve its photocatalytic activity

The high e^-/h^+ pair recombination efficiency of MoS_2 prevents it from being widely used in photocatalysis, despite the fact that it is a visible-light sensitive photocatalyst. This is a frequent problem with narrow band gap photocatalysts. Hence, to improve charge carrier separation, MoS_2 has been doped and coupled with many varied materials such as metals,[61] metal oxides,[62] and carbon-based materials.[63] Fig. 4 exhibits some of the modifications of MoS_2. The doping of MoS_2 with metal or non-metal dopants, as shown in Fig. 4a and b, can generate defects and change the optical band gap of MoS_2. Charge separation can be enhanced when associated with metals due to the existence of the metal–MoS_2 interface, as depicted in Fig. 4c. For instance, Cheah *et al.* reported an improved H_2 evolution activity of Ag@MoS_2 under irradiation by visible light.[64] They reported that the deposition of Ag onto MoS_2 assisted e^- and h^+ separation, prevented charge recombination, and hence, enhanced the overall photocatalytic performance. By creating a band offset and/or an electric field across the space-charge area at the junction between the two materials, a heterojunction enables the separation of e^-/h^+ pairs instantly. Fig. 4d shows the formation of two types of heterojunctions. A type I heterojunction results When the VB of MoS_2 is greater than the VB of the second semiconductor and the conduction band (CB) of MoS_2 is lower than the CB of the second semiconductor,

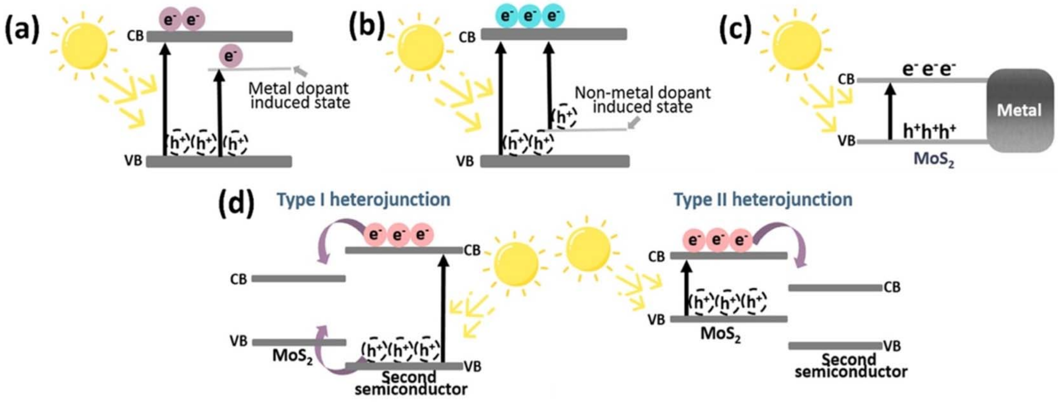

Fig. 4 Modifications of MoS_2 to improve its photocatalytic activity; (a) metal doping of MoS_2, (b) nonmetal doping of MoS_2, (c) metal deposited on MoS_2, and (d) formation of a heterojunction with a second semiconductor. Reproduced from ref. 29 with permission from [American Chemical Society], copyright [2022].

allowing both electrons and holes to pass from the second semiconductor to the MoS_2. In contrast, a type II heterojunction is created when the VB of MoS_2 is above the VB of the second semiconductor, acting as a hole sink, while the CB of the second semiconductor is below the VB of MoS_2, acting as an electron sink.[65] For example, Hu *et al.* reported that an optimized Co-doped MoS_2/g-C_3N_4 heterojuction exhibited the highest activity for the photocatalytic reduction of water, with a H_2 evolution rate of 0.31 mmol g^{-1} h^{-1}.[66] According to these authors, Co-doped MoS_2 has an edge-enriched 1T phase with more active sites than pristine MoS_2, as well as a heterojunction with g-C_3N_4 to expedite charge transfer and separation and these factors contribute to the enhanced photocatalytic activity. Additionally, the creation of ternary and quaternary chalcogenides by including one or more additional elements into binary chalcogenides is a potential method for increasing the effectiveness of charge separation and interfacial charge transfer through the addition of additional surfaces. For example, Lim *et al.* fabricated a $ZnMoS_4$/ZnO/CuS p-n heterojunction photo-catalyst that results in a hydrogen evolution rate 97% higher than an unoptimized $ZnMoS_4$/CuS p-n structure.[67]

A hydrothermal and calcination technique is used to successfully create a Z-scheme MoS_2/CuO photocatalyst that degrades 2-mercaptobenzothiazole (MBT) with excellent activity (96 percent) when exposed to visible light[68] (Fig. 5a–e).

MoS_2 nanosheets and flower-shaped CuO combine to form a Z-scheme heterostructure, which significantly boosts the separation effectiveness of photogenerated carriers. CuO and MoS_2's oxidation and reduction characteristics are enhanced by the Z-scheme electron transfer process that gives significant accumulation of photogenerated electrons and holes.

The authors proposed a possible Z-scheme charge transfer process and the reaction mechanism of MBT degradation by MoS_2/CuO heterojunction under visible light irradiation and the results are shown in Fig. 5f. Electron–hole pairs are generated by the excitation of both MoS_2 and CuO. The electrons on the CB of CuO migrate to the VB of MoS_2 and combine with holes on the VB of MoS_2. The photogenerated holes assembled by CuO can degrade MBT molecules in large quantities. In addition, due to the CB position of MoS_2 is much more negative than the potential of O_2/O_2, the electrons on the CB of MoS_2 will further undergo a reduction reaction to generate abundant O_2, which will be further involved in the degradation process. Although CuO has a higher negative VB potential than OH, it is theoretically impossible to form OH; yet, some OH has been found using the ESR technique, which may be the result of further reducing O_2. The Z-scheme charge transfer mechanism for MoS_2/CuO significantly increases the separation efficiency of photogenerated carriers and positively influences the oxidizability and reducibility of the photocatalysts. Finally, the detailed photocatalytic reaction process of the Z-scheme MoS_2/CuO heterojunction is in Fig. 5f.

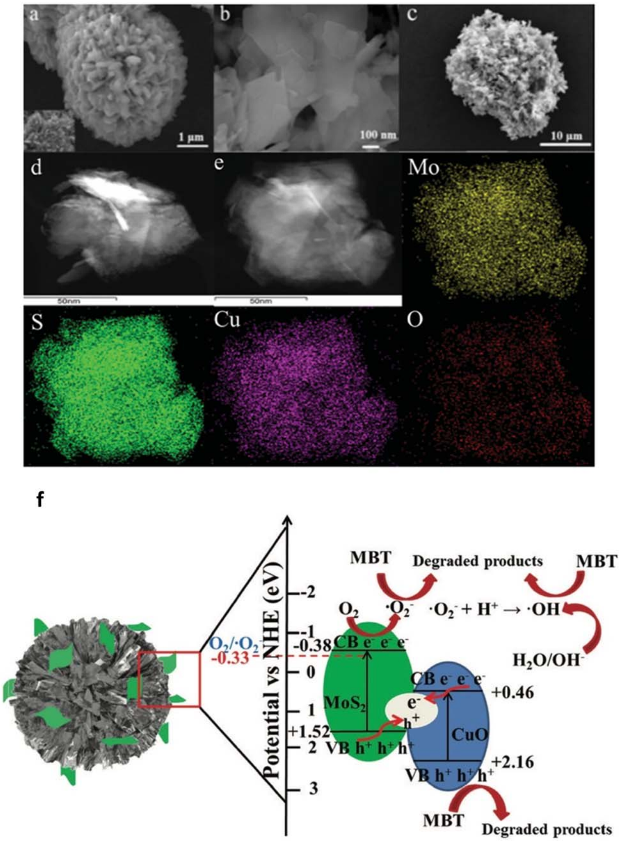

Fig. 5 (a) SEM images of CuO, (b) MoS_2, (c) MoS_2/CuO, (d) TEM image of MoS_2/CuO, (e) elemental mapping of MoS_2/CuO, (f) photocatalytic degradation mechanism of MBT over the Z-scheme MoS_2/CuO heterojunction under visible light irradiation. Reproduced from ref. 68 with permission from [Royal Society of Chemistry], copyright [2020].

A S-scheme MoS_2/g-C_3N_4 photocatalyst is developed[69] a one-pot solid-state reaction of thiourea and sodium molybdate as precursors at different temperatures under N_2 gas was applied. The variation in component contents (MoS_2 and gC_3N_4) is determined by the physicochemical characterization of the final products *via* an increase in synthesis temperature. The morphology and elemental composition of representatives were investigated using field emission scanning electron microscopy (FE-SEM), high resolution transmission electron microscopy (HR-TEM), along with energy dispersive X-ray spectroscopy (EDS) mapping (Fig. 6a–g).

The degradation of Rhodamine B in an aqueous solution under visible light was used to evaluate the enhanced photocatalytic activity of the MoS_2/gC_3N_4 composites. The best photocatalytic performance there was demonstrated by composites created at 500 °C, with a degradation efficiency of 90%, which was significantly better than that of a single g-C_3N_4. The improvement in light harvesting and the extension in the lifetime of photoinduced charge carriers of composites, which are the result of the synergistic interaction between the components, are credited with the significant improvement in photocatalytic performance. Besides, the photocatalytic mechanism is demonstrated to well-fit into the S-scheme pathway with apparent evidences (Fig. 6h).

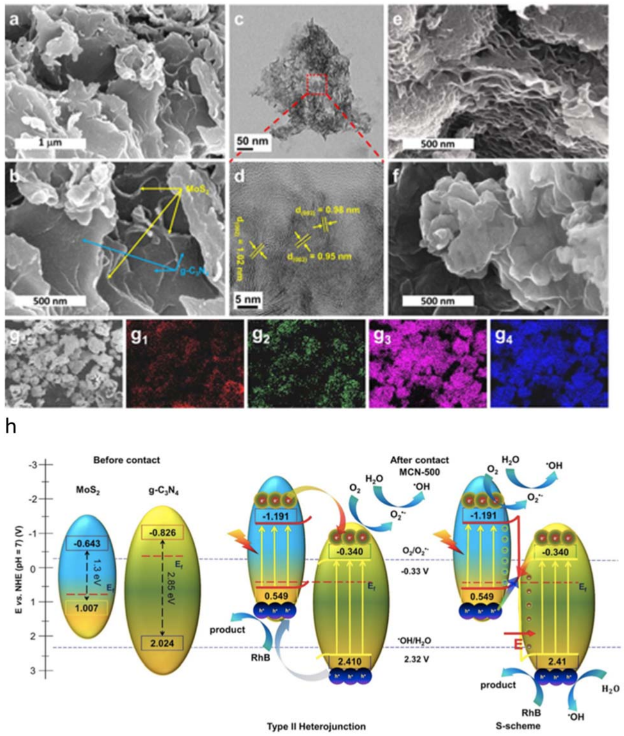

Fig. 6 (a and b) FE-SEM; and (c and d) HR-TEM images of MCN-500; FE-SEM images of (e) MCN-600; and (f) CN-500; EDS mapping images of (g) mapping area, (g_1) carbon, (g_2) nitrogen, (g_3) sulfur, and (g_4) molybdenum, (h) schematic diagram of band alignment of hetero-junction and S-scheme charge transfer on interface of MoS_2 and g-C_3N_4. Reproduced from ref. 69 with permission from [Springer Nature], copyright [2021].

6 Applications of MoS_2 based nano-photocatalyst for chemical transformations

The MoS_2 photocatalysis visible-light irradiation is considered a green alternative to traditional synthetic methodologies. As only mild conditions are needed and the formation of undesirable byproducts is decreased, it is a viable path for organic transformation processes. Summary of previous studies on photocatalytic organic transformation reactions using MoS_2-based materials are tabulated in Table 2.

6.1 Cross-dehydrogenative coupling reaction

De *et al.* developed[77a] a methodology targeted for the utilization of sacrificial amine donors for C–H functionalization with MoS_2 quantum dots (QDs) as the catalyst as well as the photosensitizer. Infact, QDs has emerged to be an active participant in the heterogeneous electron transfer process. This approach brings up new opportunities for photomediated organic transformations using nanomaterials without the need for external photosensitizers using a non-toxic, long-lasting procedure. The reduction cycle produces H_2 from water, and the oxidative cycle culminates in the CDC product. (Fig. 7).

The authors proposed a mechanistic pathway for the CDC reaction parallel to the photochemical HER mediated by MoS_2 QDs (Fig. 7). An electron is excited from the valence band (VB) to the conduction band (CB) by radiation. In presence of O_2, 2-Aryl-1,2,3,4-tetrahydroisoquinoline **1** is oxidized to radical cation $\mathbf{1}^{+\bullet}$ *via* transferring an electron to the VB to regenerate the ground state of the QD. There is no need of any external photosensitizer for the oxidation of **1**. The radical cation of **1** results the formation of iminium intermediate $\mathbf{1}^{+}$ by losing a $\mathbf{H}^{\bullet}$. The nucleophile **2** attacks the iminium intermediate $\mathbf{1}^{+}$ to give the targeted cross-coupled product **3** with simultaneous evolution of H_2. Thus, QDs act as a photosensitizer as well as a catalyst that also transfer electron for the water-splitting process and further regenerated in the process. In the proposed mechanism, they have stated that the source of H can be from H_2O as well as the nucleophile NuH. As their target was to design a methodology for the CDC reaction, they did not carry out any deuterated experiments to confirm the source of H_2.

De *et al.* also demonstrated[77b] 1T (metallic)-2H (semiconducting) phase boundaries intrinsic to individual sheets of chemically exfoliated 2D-MoS_2 that can serve as heterojunctions for enhanced photocatalysis compare to only semiconducting phase. Due to the abundance of heterojunctions in these multiphasic materials, chemically exfoliated 2D-MoS_2 provides improved stability as well as transfer of photogenerated charges to the reactants, giving better yield. Significantly, they proved that this simple synthesize material works well as a photocatalyst for the aerobic oxidative coupling of amines to imines when subjected to visible light. Given its broad applications, they believe mixed phase 2D-MoS_2 can be of interest to several industrial synthetic applications related to semiconductor-based photocatalysis. An additional benefit is that this heterogeneous photocatalyst can be regenerated up to five times without significant loss in the activity (Fig. 8).

Further De *et al.*[77c] have developed an efficient method for Cross Dehydrogenative Coupling (CDC) reaction by using mixed phase 2D-MoS_2 nanosheets and Eosin Y alongside the photochemical Hydrogen Evolution Reaction (HER). The reaction has been carried out at room temperature under visible light irradiation and results in good to excellent yields. It is an example of a CDC reaction using mixed phase 2D-MoS_2 nanosheets as a catalyst regenerator and Eosin Y as photosensitizer. Due to incomplete recovery of the catalyst, the material can be reused with slight loss in the yields. Additionally, the scope of this protocol can be used to create various C–C coupled products. This could be an illustration of how to completely utilise the oxidation and reduction cycles of several semiconductor-based photocatalysts. (Fig. 9).

6.2 Suzuki–Miyaura coupling reaction

Lim *et al.* demonstrated[78] the incorporation of MoS_2 nanosheets with Pd nanodots is a promising way for promoting the visible-light-induced Suzuki–Miyaura C–C coupling reaction. The MoS_2 nanosheets decorated with Pd nanodots showed excellent photocatalytic activity. The turnover frequency for the biphenyl product was >1600 h^{-1} even under sunlight illumination at

Table 2 Summary of previous studies on photocatalytic chemical transformation reactions using MoS_2-based materials

S. N.	Application	Photocatalyst used	Morphology	Particle size	Light source	Performance	Ref.
1	Photocatalytic oxidation of benzyl alcohol to benzaldehyde	Co-doped MoS_2/g-C_3N_4	2D nanosheet morphology with curly stripes		80 W LED lamp	Benzaldehyde production rate of 0.48 mmol g^{-1} h^{-1}	66
2	Photocatalytic oxidative coupling of thiols	Pd@Cu/MoS_2	Spherical	64.5 nm	300 W Xe lamp	~99% conversion under 400–800 nm irradiation	70
3	Photocatalytic reduction of 4-nitrophenol	TiO_2 hollow spheres/crumpled MoS_2 nanosheet	Hollow sphere	~200 nm	500 W Xe lamp	99.35% photocatalytic reduction of 4-nitrophenol	71
4	Photocatalytic conversion of CO_2 to methane	MoS_2/Cu	MoS_2 nanosheets are coated on the surface of Cu nanorods	About 50–700 nm	300 W Xe lamp	Maximum yield of methane ~23 mmol g^{-1} h^{-1}	72
5	Photocatalytic reduction of CO_2 to methanol	MoS_2 grown on hexagonal boron nitride nanoplatelets	MoS_2 nanosheets are uniformly grown over the hexagonal boron nitride nanoplatelets	Each MoS_2 nanosheet is composed of 2–6 molecular lamellae	20 W white LED lamp	Maximum yield of methanol 5994 μmol g^{-1}	73
6	Photocatalytic reduction of CO_2 to methane and CO	In_2S_3/MoO_3@MoS_2	Distorted hexagonal nanorods		300 W Xe lamp	Yield ~29.4 and ~35.6 μmol g^{-1} h^{-1} for CH_4 and CO, respectively	74
7	Photocatalytic selective oxidation of benzyl alcohols to benzaldehyde	Ag_3PO_4 nanoparticle@MoS_2 quantum dot/few-layered MoS_2 nanosheet	Nanosheet		300 W Xe lamp	≤92% conversion of benzyl alcohol and ~87% yield of benzaldehyde after 3 h of irradiation	75
8	Photocatalytic reduction of 4- nitrophenol to 4-aminophenol	CdS-MoS_2/rGO composite	Flowerlike morphology		500 W Xe lamp	≤70% reduction of 4-nitrophenol after 60 min of irradiation	76

room temperature. Mechanistic researches revealed that the high catalytic activity of MoS_2 originated from the efficient electron–hole pair generation mechanism under visible-light (Fig. 10).

6.3 Photocatalytic NH_3 synthesis

He *et al.* developed[79] the efficient photoreduction of N_2 to NH_3 over ternary MoS_2/C–ZnO composite, that was prepared *via* a combination of hydrothermal and photodeposition method (Fig. 11).

Several methods were employed to characterise the produced composite, and the results displayed that carbon was loaded onto the surface of ZnO instead of doped into the lattice in order to prevent charge carrier recombination. By thermal processing, the carbon content of C–ZnO can be altered by which enhances the effectiveness of charge separation. For calcination, the most favourable temperature of 300 °C determined. The separation of electron–hole pairs can be further improved by photodepositing MoS_2 nanoparticles on the C-ZnO-300 sample, which traps electrons on the carbon layer. The ideal 1% MoS_2/C-ZnO-300 composite exhibits the fastest NH_3 generation rate under simulated sunlight irradiation at 245.7 μmol L^{-1} g^{-1} h^{-1}, which is 9.3 and 4.0 times higher than that of ZnO and C–ZnO, respectively. However, when exposed to visible light, C–ZnO performs best, producing NH_3 at a rate of 28.8 μmol L^{-1} g^{-1} h^{-1}, indicating that the composite employs a different process. The carbon layer was thought to act as a photosensitizer by transferring electrons to ZnO or MoS_2. The processes proposed have been confirmed by EIS and PC evaluations. The addition of a carbon layer and MoS_2 nanoparticles to the ZnO increases the BET area. The increased surface area might be partially responsible for the higher photocatalytic performance. (Fig. 11a and b). There is another way to reduce N_2 to NH_3 *via* photocatalysis[80,81].

6.4 Photoelectrochemical nitrogen reduction

The photoelectrochemical (PEC) technique, which uses both solar energy as well as electricity efficiently synthesize ammonia under ambient conditions. Han *et al.*[82] have been synthesized MoS_2@LZO heterostructures by assembling 2D-MoS_2 nanoflakes on $La_2Zr_2O_7$ nanofibers *via* a facile hydrothermal method (Fig. 12a).

Due to the electrical dispersion in LZO, the homogeneous assembly of MoS_2@LZO prevents the photogenerated electron hole pair from recombining more quickly. Superior PEC-NRR performances can be seen as a result of the interaction between the localised electronic distribution in the MoS_2@LZO heterostructures, oxygen vacancies in $La_2Zr_2O_7$, excellent conductivity of the nanofibers, and increased exposure of surface sites for electron–hole generation in MoS_2. The trapped photoelectron during N_2 activation is donated by the reduction of N_2 to NH_3 at the oxygen vacancy, which serves as the

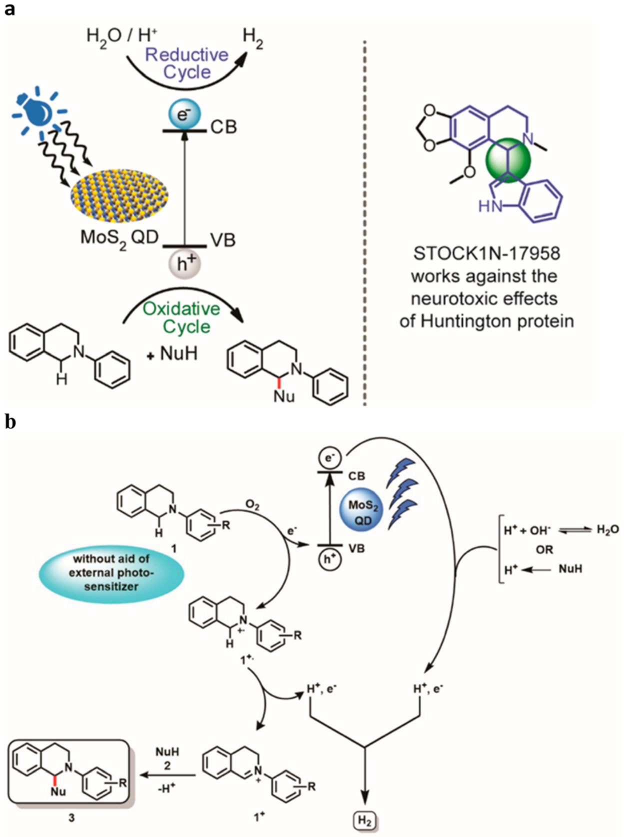

Fig. 7 (a) Photomediated oxidation and reduction cycle of MoS_2 QDs. (b) Proposed mechanism for the catalytic activity of MoS_2 blue QDs in CDC reaction synchronized with HER. Reproduced from ref. 77*a* with permission from [American Chemical Society], copyright [2022].

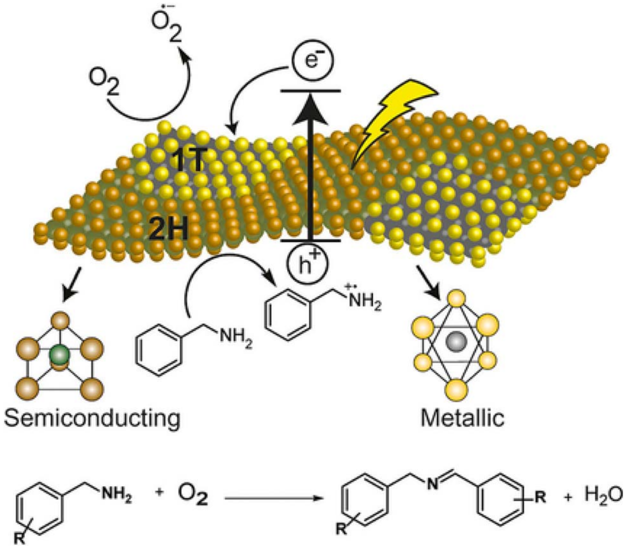

Fig. 8 Plausible mechanism for the oxidative coupling of benzylamine to imine photocatalyzed by mixed-phase 2D-MoS_2 nanosheets. Reproduced from ref. 77*b* with permission from [John Wiley & Sons, Inc.], copyright [2018].

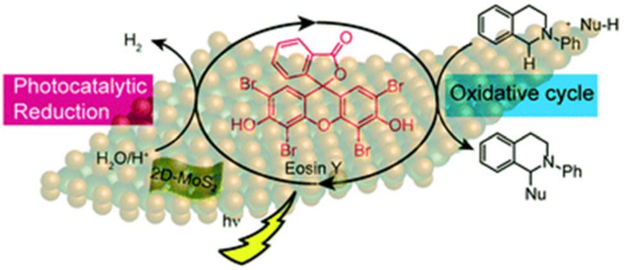

Fig. 9 Schematic illustration of the 2D-MoS_2 photocatalyzed oxidation and reduction cycles in presence of Eosin Y as photosensitizer. Reduction cycle produces H_2 from water as reported earlier, whereas oxidative cycle is responsible for CDC Reaction and formation of additional H_2. Reproduced from ref. 77*c* with permission from [Royal Society of Chemistry], copyright [2019].

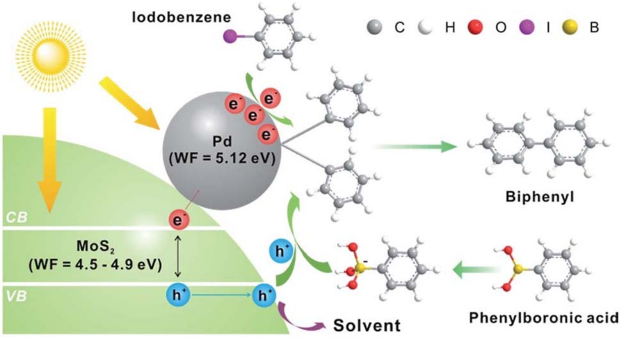

Fig. 10 The Pd-nanodot decorated MoS_2 micro/nanosheet for an efficient visible light induced photocatalytic Suzuki–Miyaura coupling reaction. Reproduced from ref. 78 with permission from [Royal Society of Chemistry], copyright [2017].

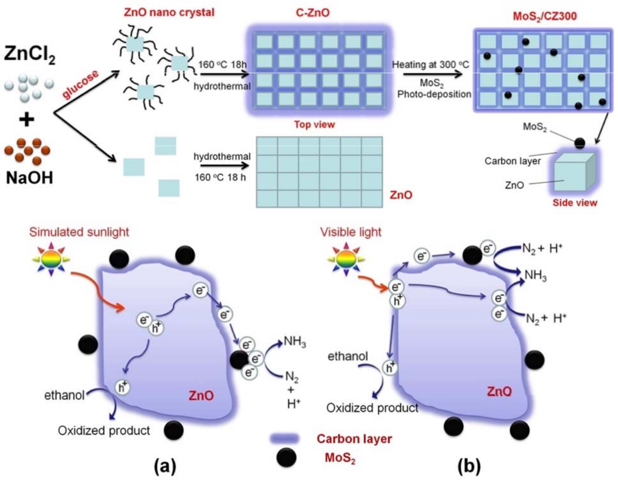

Fig. 11 Preparation of MoS_2/CZ300 photocatalyst and the suggested charge transfer mechanism of MoS_2/CZ300 composite (a) under simulated sunlight (b) and visible light irradiation. Reproduced from ref. 79 with permission from [American Chemical Society], copyright [2018].

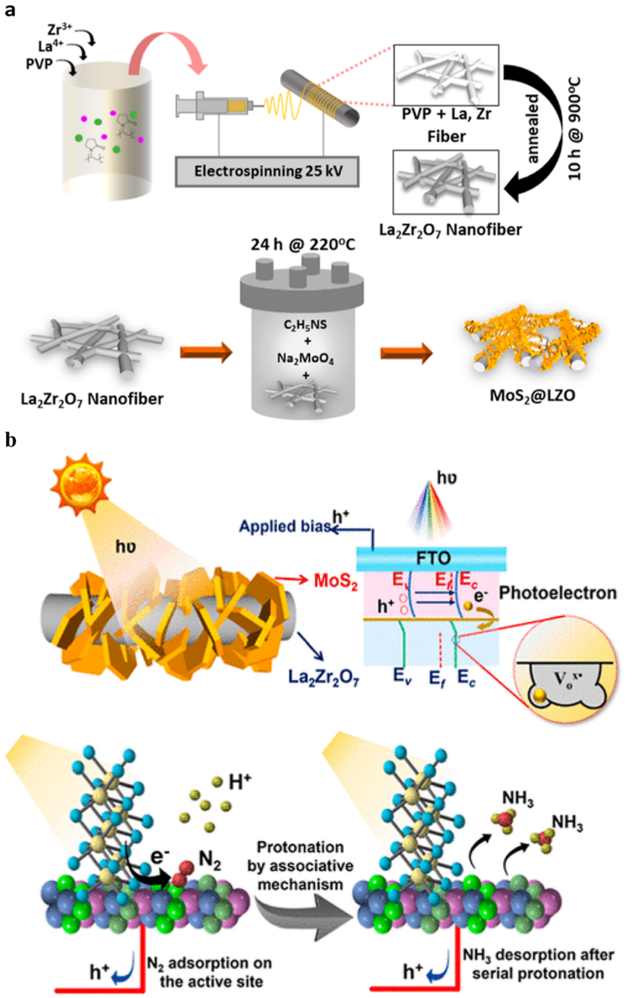

Fig. 12 (a) Schematic illustration of the electrospun LZO nanofibers, followed by hydrothermal synthesis of MoS_2@ LZO. (b) The band structure demonstrating the type II heterojunction for MoS_2@LZO heterostructures with a reduced Fermi level under applied bias and solar illumination and schematic illustration of the PEC-NRR mechanism following the associative pathway for ammonia production. Reproduced from ref. 82 with permission from [American Chemical Society], copyright [2022].

active site for these reactions. The MoS_2@LZO PEC catalyst exhibits a maximum ammonia yield rate of approximately 10.4 μg h^{-1} cm^{-2} and a higher faradaic efficiency of approximately 2.25% compared to pristine MoS_2 and LZO. The heterostructure interface, which is rich in oxygen vacancies and offers a stable design with effective active sites, can be used to confirm this remarkable performance. Compared to the current MoS_2 catalysts, MoS_2@LZO demonstrates a higher ammonia yield, selective N_2 adsorption, and excellent stability. The 2D-MoS_2 nanoflakes, the $La_2Zr_2O_7$ pyrochlore/fluorite structured nanofibers, and their heterostructure interfaces for enhanced ammonia production are presented with PEC-NRR mechanisms under ambient conditions. For various additional catalysis techniques to efficiently drive photoelectrocatalytic activity, the design strategy of inserting an n-type semiconductor over rich oxygen-vacant stable nanostructures to establish an interface can be used. (Fig. 12b).

6.5 Photocatalytic oxidation of nitrite

Zheng *et al.* reported[83] the photocatalytic oxidation rate of NO_2^-under simulated solar irradiation, which can reach 62% by the MoS_2/TiO_2 composite synthesized in a hydrothermal system with a C_2H_5NS/Na_2MoO_4 molar ratio of 1 : 0.6 : under 200 °C for 24 h, which is significantly higher than that by pristine TiO_2 NFs, P25 and pure MoS_2. The photocatalytic oxidation process of NO_2^- follows the Langmuir–Hinshelwood kinetic model (pseudo-first order reaction), and the reaction rate constant (k) of the as-prepared composite is about 0.19194 h^{-1}. MoS_2 considerably increases the ability of catalyst ability to absorb visible light, which promotes the production of electrons and holes and ensures the strong photoactivity of catalyst. The composite has an about 2.2 eV band gap, which indicates improved visible light absorption. The titanium substrate is permanently attached to the composite using this straightforward, low-consumption approach, enabling recycling and ecologically responsible implementation possible (Fig. 13).

6.6 Photocatalytic conversion of CO_2 and H_2O to CO, CH_4 and H_2 products

Ray *et al.* reported,[84] theintegration of photoabsorber MoS_2 and N-containing conducting polymer polypyrrole (PPy) over reduced graphene oxide improved CO_2 photoreduction and H_2 production (rGO). A variety of rGO-MoS/PPy nanocomposites were created and morphologically, structurally, and optically studied using various methods. Under pretend sunlight the optimal rGO-MoS /PPynanocomposite was found to exhibit a remarkable production of CO (3.9 μmol g^{-1} h^{-1}), CH_4 (1.50 μmol g^{-1} h^{-1}), and H_2 (4.19 μmol g^{-1} h^{-1}) in the photocatalytic reduction of CO_2 in an aqueous suspension (Fig. 14).

The synergistic effect of the MoS_2, rGO, and PPy nanostructures, which encouraged the separation and migration of the photogenerated charges through the heterojunction interfaces and decreased electron–hole recombination, was

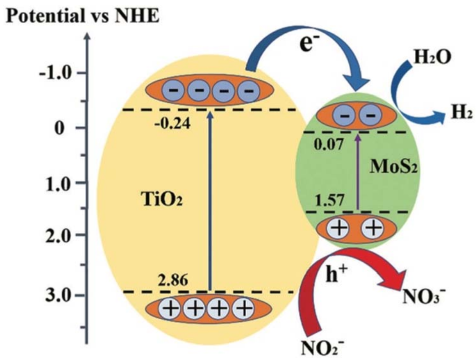

Fig. 13 Schematic illustration of the energy band structure and electron–hole separation of MoS_2/TiO_2 composites. Reproduced from ref. 83 with permission from [Royal Society of Chemistry], copyright [2021].

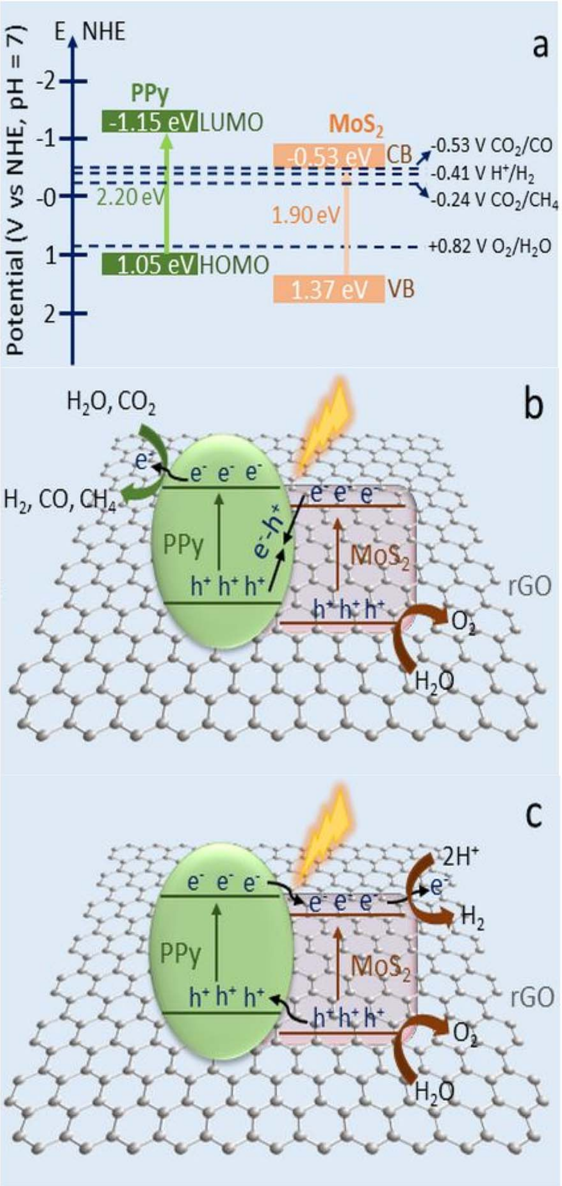

Fig. 14 (a) Schematic representation of the band positions and potentials of PPy and MoS_2. (b) Photocatalytic CO_2 conversion into CH_4 and CO gas *via* Z-scheme mechanism with rGO as redox mediator on the rGO-MoS_2/PPy nanocomposite. (c) The conventional type II electron transfer for H_2 production on the rGO-MoS_2/PPy nanocomposite. Reproduced from ref. 84 with permission from [American Chemical Society], copyright [2020].

attributed to the improvement in the photocatalytic performance of the highly active surface material rGO-MoS_2/PPy-150. The PPy in the rGO-MoS_2/PPy nanocomposite played multiple roles in improving the photocatalytic reduction of CO due to its superior conductivities, CO_2 adsorption capabilities *via* its amine groups, and electron storage qualities. Better catalytic performance is possible due to the reduced PPy concentration in nanocomposite. Importantly, the strong recycling performance of rGO-MoS_2/PPy-150 nanocomposite revealed the robustness and stability of photocatalyst (Fig. 14a–c).

7 Future outlook

Although many studies have focused on the synthesis of MoS_2 and MoS_2-based nanomaterials and their different uses, there are still a plethora of challenges:

1. MoS_2-based materials will be extensively used in a variety of disciplines and could one day become commercially feasible because of their unique physical and chemical qualities. With this, MoS_2 will be applied to various media and released into the environment, potentially posing risks to both human health and the ecosystem. Therefore, a detailed evaluation of the toxicity of MoS_2-based compounds is required.

2. The application of MoS_2-based photocatalysts has so far been confined to laboratory-based research; it has not yet been investigated how well MoS_2 performs in real-world environments, and a perfect photocatalyst that can be used on a wide scale and in industry has not yet been developed.

3. Certain MoS_2 composites become unstable when exposed to visible light. Therefore, more investigation is required to design materials based on MoS_2 that are photosensitive.

4. A significant challenge pertains for the development of practical techniques for the generation of MoS_2 in quantities appropriate for industrial applications. For large-scale production, additional research into the scaling up of synthetic approaches is therefore needed.

8 Conclusion

In this review, we highlighted the different MoS_2 structures, their synthesising techniques and properties. The primary benefits and drawbacks of synthesis approaches were also summarised. MoS_2 is a promising material with a wide range of applications. MoS_2 and MoS_2-based nanomaterials are currently the topic of extensive research as promising photocatalyst for the photocatalytic degradation and inorganic and organic chemical transformation. MoS_2 and MoS_2-based materials have exceptional physicochemical features, due to which they exhibit wide range of synthetic applications like coupling reaction, oxidation, reduction as well as organic and inorganic compound production. This review relies on recent developments regarding the application of MoS_2 in chemical transformations. The prospects for successful visible-light-induced photocatalysis using MoS_2 based materials are finally discussed.

Conflicts of interest

There are no conflicts to declare.

References

1 A. Majumder, D. Saidulu, A. K. Gupta and P. S. Ghosal, *J. Environ. Manage.*, 2011, **293**, 112858.
2 A. L. Camargo-Perea, E. A. Serna-Galvis, J. Lee and R. A. Torres-Palma, *Ultrason. Sonochem.*, 2021, **73**, 105500.
3 Y. Rao, D. Xue, H. Pan, J. Feng and Y. Li, *Chem. Eng. J.*, 2016, **283**, 65–75.

4 M. H. F. Graumans, W. F. L. M. Hoeben, M. F. P. van Dael, R. B. M. Anzion, F. G. M. Russel and P. T. J. Scheepers, *Environ. Res.*, 2021, **195**, 110884.

5 P. Sharma, D. Kumar and S. Mutnuri, *J. Pharm. Anal.*, 2021, **11**, 320–329.

6 Q. Zhou, Y. Huang, Y. Zhang, C. Xu, W. Huang, K. Yang, X. Chen and Y. Zhang, *Mater. Chem. Phys.*, 2020, **276**, 125333.

7 Md. Ahmaruzzaman and V. Gadore, *J. Environ. Chem. Eng.*, 2021, **9**, 105836.

8 (*a*) X. Li, R. Shen, S. Mab, X. Chen and J. Xie, *Appl. Surf. Sci.*, 2018, **430**, 53–107; (*b*) E. Canadell, A. L. Beuze, M. A. E. Khalifa, R. Chevrel and M. H. Whangbo, *J. Am. Chem. Soc.*, 1989, **111**, 3778–3782; (*c*) J. N. Coleman, M. Lotya, A. O'Neil', S. D. Bergin, P. J. King, U. Khan, K. Young, A. Gaucher, S. De and R. J. Smith, *Science*, 2011, **331**, 568–571.

9 F. Guo, X. Huang, Z. Chen, H. Ren, M. Li and L. Chen, *J. Hazard. Mater.*, 2020, **390**, 12215.

10 R. N. Dalila, M. K. Md Arshad, S. C. B. Gopinath, W. M. W. Norhaimi and M. F. M. Fathil, *Biosens. Bioelectron.*, 2019, **132**, 248–264.

11 Y. Yuan, R. T. Guo, L. F. Hong, X. Y. Ji, Z. S. Li, Z. D. Lin and W. G. Pan, *Colloids Surf. A Physicochem. Eng. Asp.*, 2021, **611**, 125836.

12 S. Ni, L. Yang, H. Qu, X. Zhu, Z. Xu, M. Yuan, H. Xing, L. Wang, J. Yu and H. Liu, *J. Environ. Chem. Eng.*, 2021, **9**, 105101.

13 L. Cheng, W. Huang, Q. Gong, C. Liu, Z. Liu, Y. Li and H. Dai, *Angew. Chem., Int. Ed.*, 2014, **53**, 7860–7863.

14 S. Yin, Y. Ding, C. Luo, Q. Hu, Y. Chen, J. Di, B. Wang, J. Xia and H. Li, *Colloids Surf. A*, 2021, **609**, 125655.

15 L. Liu, J. Cao, M. Ali, J. Zhang and Z. Wang, *Environ. Adv.*, 2021, **4**, 100059.

16 M. Arumugam, Y. Yu, H. J. Jung, S. Yeon, H. Lee, J. Theerthagiri, S. J. Lee and M. Y. Choi, *Environ. Res.*, 2021, **197**, 111080.

17 (*a*) H. Wang, C. Li, P. Fang, Z. Zhang and J. Z. Zhang, *Chem. Soc. Rev.*, 2018, **47**, 6101–6127; (*b*) P. R. Sivaranjani, B. Janani, A. M. Thomas, L. L. Raju and S. S. Khan, *J. Cleaner Prod.*, 2022, **352**, 131506; (*c*) M. H. Wu, L. Li, N. Liu, D. J. Wang, Y. C. Xue and L. Tang, *Process Saf. Environ. Prot.*, 2018, **118**, 40–58; (*d*) K. F. Mak, C. Lee, J. Hone, J. Shan and T. F. Heinz, *Phys. Rev. Lett.*, 2010, **105**, 136805; (*e*) Y. Yuan, R.-t. Guo, L.-f. Hong, X.-y. Ji, Z.-s. Li, Z.-d. Lin and W.-g. Pan, *Colloids Surf., A*, 2021, **611**, 125836; (*f*) B. Han and Y. H. Hu, *Energy Sci. Eng.*, 2016, **4**, 285e304; (*g*) M.-h. Wu, L. Li, N. Liu, D.-j. Wang, Y.-c. Xue and L. Tang, *Process Saf. Environ. Prot.*, 2018, **118**, 40e58; (*h*) X. Meng, Z. Li, H. Zeng, J. Chen and Z. Zhang, *Appl. Catal. B: Environ.*, 2017, **210**, 160e172; (*i*) G. Zhang, H. Liu, J. Qu and J. Li, *Energy Environ. Sci.*, 2016, **9**, 1190e1209; (*j*) J. Theerthagiri, R. A. Senthil, B. Senthilkumar, A. Reddy Polu, J. Madhavan and M. Ashokkumar, *J. Solid State Chem.*, 2017, **252**, 43e71; (*k*) Z. Li, X. Meng and Z. Zhang, *J. Photochem. Photobiol. C*, 2018, **35**, 39e55; (*l*) Z. Liang, R. Shen, Y. H. Ng, P. Zhang, Q. Xiang and X. Li, *J. Mater. Sci. Technol.*, 2020, **56**, 89e121; (*m*) D. B. Sulas-Kern, E. M. Miller and J. L. Blackburn, *Energy Environ. Sci.*, 2020, **13**, 2684e2740; (*n*) N. Thomas, S. Mathew, K. M. Nair, K. O'Dowd, P. Forouzandeh, A. Goswami, G. McGranaghan and S. C. Pillai, *Mater. Today Sustain.*, 2021, **13**, 100073.

18 (*a*) V. Srivastava, P. K. Singh and P. P. Singh, *Croat. Chem. Acta*, 2015, **88**(1), 59–65; (*b*) V. Srivastava, P. K. Singh and P. P. Singh, *Croat. Chem. Acta*, 2015, **88**(3), 227–233; (*c*) V. Srivastava, P. K. Singh and P. P. Singh, *Asian J. Chem.*, 2016, **28**(10), 2159–2163; (*d*) V. Srivastava, P. K. Singh and P. P. Singh, *Croat. Chem. Acta*, 2017, **90**(3), 435–441; (*e*) V. Srivastava, P. K. Singh, S. Kanaujia and P. P. Singh, *New J. Chem.*, 2018, **42**, 688; (*f*) P. K. Singh, P. P. Singh and V. Srivastava, *Croat. Chem. Acta*, 2018, **91**(3), 383–387; (*g*) V. Srivastava, P. K. Singh and P. P. Singh, *Tetrahedron Lett.*, 2019, **60**, 40–43; (*h*) V. Srivastava, P. K. Singh and P. P. Singh, *Tetrahedron Lett.*, 2019, **60**, 1333–1336; (*i*) V. Srivastava, P. K. Singh and P. P. Singh, *Tetrahedron Lett.*, 2019, **60**, 151041; (*j*) V. Srivastava, P. K. Singh and P. P. Singh, *Rev. Roum. Chim.*, 2020, **65**(3), 221–226.

19 (*a*) V. Srivastava and P. P. Singh, *RSC Adv.*, 2017, **7**, 31377–31392; (*b*) V. Srivastava, P. K. Singh, A. Srivastava and P. P. Singh, *RSC Adv.*, 2020, **10**, 20046; (*c*) A. Srivastava, P. K. Singh, A. Ali, P. P. Singh and V. Srivastava, *RSC Adv.*, 2020, **10**, 39495; (*d*) V. Srivastava, P. K. Singh, A. Srivastava and P. P. Singh, *RSC Adv.*, 2021, **11**, 14251–14259; (*e*) V. Srivastava and P. P. Singh, *Org. Biomol. Chem.*, 2021, **19**, 313–321; (*f*) P. P. Singh, P. K. Singh, M. Z. Beg, A. Kashyap and V. Srivastava, *Synth. Commun.*, 2021, **51**(20), 3033–3058; (*g*) V. Srivastava, P. K. Singh, A. Srivastava, S. Sinha and P. P. Singh, *Photochem*, 2021, **1**, 237–246; (*h*) V. Srivastava, P. K. Singh, S. Tivari and P. P. Singh, *Org. Chem. Front.*, 2022, **9**, 1485; (*i*) V. Srivastava, P. K. Singh and P. P. Singh, *J. Photochem. Photobiol., C*, 2022, **50**, 100488; (*j*) V. Srivastava and P. P. Singh, *RSC Adv.*, 2022, **12**, 18245.

20 M. Alam Khan and Y. M. Kang, Synthesis and Electrochemical Performance of Colloidal MoS_2 Nanosheets as an Anode Material in Sodium Ion Battery, *J. Energy Storage*, 2016, 252–257.

21 H. K. Sadhanala, S. Senapati, K. V. Harika, K. K. Nanda and A. Gedanken, *New J. Chem.*, 2018, **42**(17), 14318–14324.

22 J. S. Roy, G. Dugas, S. Morency and Y. Messaddeq, *Phys. Rev. E*, 2020, **120**, 114114.

23 N. Fahimi-Kashani, A. Rashti, M. R. Hormozi-Nezhad and V. Mahdavi, *Anal. Methods*, 2017, **9**(4), 716–723.

24 W. Chen, M. Liu, S. Wei, X. Li, L. Mao and W. Shangguan, *J. Alloys Compd.*, 2020, **836**, 155401.

25 C. Nagaraju, C. V. V. Muralee Gopi, J. W. Ahn and H. J. Kim, *New J. Chem.*, 2018, **42**(15), 12357–12360.

26 W. Gu, Y. Yan, C. Zhang, C. Ding and Y. Xian, *ACS Appl. Mater. Interfaces*, 2016, **8**(18), 11272–11279.

27 S. V. Prabhakar Vattikuti, C. Byon, C. Venkata Reddy, B. Venkatesh and J. Shim, *J. Mater. Sci.*, 2015, **50**(14), 5024–5038.

28 W. Chen, L. Sun, Q. Li, L. Huo and H. Zhao, *Int. J. Hydrogen Energy*, 2020, **45**(43), 22459–22468.

29 A. Rahman, J. R. Jennings, A. L. Tan and M. M. Khan, *ACS Omega*, 2022, 7(26), 22089–22110.

30 N. Tian, Z. Li, D. Xu, Y. Li, W. Peng, G. Zhang, F. Zhang and X. Fan, *Ind. Eng. Chem. Res.*, 2016, **55**(32), 8726–8732.

31 J. H. Kim, J. Lee, S. Park, C. Seo, S. J. Yun, G. H. Han, J. Kim, Y. H. Lee and H. S. Lee, *Curr. Appl. Phys.*, 2022, **33**, 59–65.

32 H. Lin, C. Wang, J. Wu, Z. Xu, Y. Huang and C. Zhang, *New J. Chem.*, 2015, **39**(11), 8492–8497.

33 X. Li, A. Tang, J. Li, L. Guan, G. Dong and F. Teng, *Nanoscale Res. Lett.*, 2016, **11**(1), 171.

34 (*a*) Y. Liu, Q. Zhong, K. Chen, J. Zhou, X. Yang and W. Chen, *J. Mater. Sci.: Mater. Electron.*, 2017, **28**(18), 13633–13637; (*b*) L. Liu, Z. Huang, Y. Peng and P. Huang, *New J. Chem.*, 2017, **41**(15), 7674–7680.

35 L. Liu, Z. Huang, Y. Peng and P. Huang, *New J. Chem.*, 2017, **41**(15), 7674–7680.

36 L. Li, Z. Guo, S. Wang, D. Li, X. Hou, F. Wang, Y. Yang and X. Yang, *Anal. Methods*, 2019, **11**(26), 3307–3313.

37 B. Sheng, J. Liu, Z. Li, M. Wang, K. Zhu, J. Qiu and J. Wang, *Mater. Lett.*, 2015, **144**, 153–156.

38 S. Huang, C. Chen, H. Tsai, J. Shaya and C. Lu, *Sep. Purif. Technol.*, 2018, **197**, 147–155.

39 X. Zhang, H. Suo, R. Zhang, S. Niu, X. qi Zhao, J. Zheng and C. Guo, *Mater. Res. Bull.*, 2018, **100**, 249–253.

40 M. Sabar, U. Amara, S. Riaz, A. Hayat, M. Nasir and M. H. Nawaz, *Mater. Lett.*, 2022, **308**, 131233.

41 Y. Cai, L. Niu, X. Liu, Y. Zhang, Z. Zheng, L. Zeng and A. Liu, *J. Hazard. Mater.*, 2022, **425**, 128053.

42 X. Yu, Y. Meng, Y. Yan, X. Jin, G. Ni and J. Peng, *Microchem. J.*, 2020, **152**, 104406.

43 U. Chothe, C. Ugale, M. Kulkarni and B. Kale, *Crystals*, 2021, **11**(6), 660.

44 S. Singh, A. Modak, K. Ki. Pant, A. Sinhamahapatra and P. Biswas, *ACS Appl. Nano Mater.*, 2021, **4**(9), 8644–8667.

45 V. Singh and S. Rath, *Syst. Nanostruct.*, 2021, **128**, 114617.

46 V. Hasija, P. Raizada, V. K. Thakur, A. A. P. Khan, A. M. Asiri and P. Singh, *J. Environ. Chem. Eng.*, 2020, **8**, 104307.

47 M. Guo, Z. Xing, T. Zhao, Y. Qiu, B. Tao, Z. Li and W. Zhou, *Appl. Catal. B Environ.*, 2020, **272**, 118978.

48 K. Talukdar, K. Saravanakumar, Y. Kim, A. Fayyaz, G. Kim, Y. Yoon and C. M. Park, *Composites Part B*, 2021, **215**, 108780.

49 L. Luo, M. Shi, S. Zhao, W. Tan, X. Lin, H. Wang and F. Jiang, *J. Saudi Chem. Soc.*, 2021, **23**, 762–773.

50 X. Bai, H. Lv, Z. Liu, J. Chen, J. Wang, B. Sun, Y. Zhang, R. Wang and K. Shi, *J. Hazard. Mater.*, 2021, **416**, 125830.

51 J. Singh, S. R. Kumar and R. K. Soni, *J. Alloys Compd.*, 2020, **849**, 156502.

52 H. Jing, *Chem. Phys.*, 2021, **548**, 111241.

53 M. Nazifi, A. M. Ramezani, G. Absalan and R. Ahmadi, *Sens. Actuators, B*, 2021, **332**, 129459.

54 A. Neetika Kumar, R. Chandra and V. K. Malik, *Thin Solid Films*, 2021, **725**, 138625.

55 Y. Jiao, Q. Huang, J. Wang, Z. He and Z. Li, *Appl. Catal., B*, 2019, **247**, 124–132.

56 (*a*) A. Cepellotti, G. Fugallo, L. Paulatto, M. Lazzeri, F. Mauri and N. Marzari, *Nat. Commun.*, 2015, **6**, 6400; (*b*) G. Fugallo, A. Cepellotti, L. Paulatto, M. Lazzeri, N. Marzari and F. Mauri, *Nano Lett.*, 2014, **14**, 6109–6114; (*c*) X. Xu, L. F. C. Pereira, Y. Wang, J. Wu, K. Zhang, X. Zhao, S. Bae, C. T. Bui, R. Xie, J. T. L. Thong, B. H. Hong, K. P. Loh, D. Donadio, B. Li and B. Ozyilmaz, *Nat. Commun.*, 2014, **5**, 3689; (*d*) S. Ghosh, W. Bao, D. L. Nika, S. Subrina, E. P. Pokatilov, C. N. Lau and A. A. Balandin, *Nat. Mater.*, 2010, **9**, 555–558; (*e*) A. A. Balandin, S. Ghosh, W. Bao, I. Calizo, D. Teweldebrhan, F. Miao and C. N. Lau, *Nano Lett.*, 2008, **8**, 902–907; (*f*) A. A. Balandin, *MRS Bull.*, 2014, **39**, 817–823; (*g*) A. Branny, S. Kumar, R. Proux and B. D. Gerardot, *Nat. Commun.*, 2017, **8**, 15053; (*h*) C. Palacios-Berraquero, D. M. Kara, A. R. P. Montblanch, M. Barbone, P. Latawiec, D. Yoon, A. K. Ott, M. Loncar, A. C. Ferrari and M. Atatüre, *Nat. Commun.*, 2017, **8**, 15093; (*i*) S. Kumar, A. Kaczmarczyk and B. D. Gerardot, *Nano Lett.*, 2015, **15**, 7567–7573; (*j*) J. Kern, I. Niehues, P. Tonndorf, R. Schmidt, D. Wigger, R. Schneider, T. Stiehm, S. Michaelis de Vasconcellos, D. E. Reiter, T. Kuhn and R. Bratschitsch, *Adv. Mater.*, 2016, **28**, 7101–7105; (*k*) G. D. Shepard, O. A. Ajayi, X. Li, X. Y. Zhu, J. Hone and S. Strauf, *2D Mater.*, 2017, **4**, 21019; (*l*) N. Morell, A. Reserbat-Plantey, I. Tsioutsios, K. G. Schädler, F. Dubin, F. H. L. Koppens and A. Bachtold, *Nano Lett.*, 2016, **16**, 5102–5108; (*m*) C. H. Liu, I. S. Kim and L. J. Lauhon, *Nano Lett.*, 2015, **15**, 6727–6731; (*n*) J. Lee, Z. Wang, K. He, J. Shan and P. X. L. Feng, *ACS Nano*, 2013, **7**, 6086–6091; (*o*) J. Chaste, A. Missaoui, S. Huang, H. Henck, Z. B. Aziza, L. Ferlazzo, A. Balan, A. T. C. Johnson, R. Braive and A. Ouerghi, *ACS Nano*, 2018, **12**, 3235–3242; (*p*) B. Bagchi, N. A. Hoque, N. Janowicz, S. Das and M. K. Tiwari, *Nano Energy*, 2020, **78**, 1053.

57 X. Hou, H. Jiang, M. K. A. Ali, H. Liu, D. Su and Z. Tian, *J. Mol. Liq.*, 2020, **311**, 113303.

58 Z. Bojarska, J. Kopytowski, M. Mazurkiewicz-Pawlicka, P. Bazarnik, S. Gierlotka, A. Rozen and L. Makowski, *Tribol. Int.*, 2021, **160**, 106999.

59 S. Kaushik, U. K. Tiwari, S. S. Pal and R. K. Sinha, *Biosens. Bioelectron.*, 2019, **126**, 501–509.

60 K. Peng, J. Wang, H. Wang, X. Li, P. Wan, H. Zhang and L. Bai, *Appl. Clay Sci.*, 2019, **183**, 105346.

61 M. Ikram, M. I. Khan, A. Raza, M. Imran, A. Ul-Hamid and S. Ali, *Phys. Rev. E*, 2020, **124**, 114246.

62 Ritika, M. Kaur, A. Umar, S. Mehta, S. Singh, S. Kansal, H. Fouad and O. Alothman, *Materials*, 2018, **11**(11), 2254.

63 M. Wang, P. Ju, J. Li, Y. Zhao, X. Han and Z. Hao, *ACS Sustainable Chem. Eng.*, 2017, **5**(9), 7878–7886.

64 A. J. Cheah, W. S. Chiu, P. S. Khiew, H. Nakajima, T. Saisopa, P. Songsiririthigul, S. Radiman and M. A. A. Hamid, *Catal. Sci. Technol.*, 2015, **5**(8), 4133–4143.

65 S. San Martín, M. J. Rivero and I. Ortiz, *Catalysts*, 2020, **10**(8), 901.

66 Y. Hu, X. Yu, Q. Liu, L. Wang and H. Tang, *Carbon*, 2022, **188**, 70–80.

67 W. Y. Lim, H. Wu, Y. F. Lim and G. W. Ho, *J. Mater. Chem. A*, 2018, **6**(24), 11416–11423.

68 Y. Wang, X. Tang, Z. Liu, Y. Yan, B. Yang and Z. Zhu, *New J. Chem.*, 2020, **44**, 18264–18273.

69 H. Tran Huu, M. D. N. Thi, V. P. Nguyen, *et al.*, *Sci. Rep.*, 2021, **11**, 14787.

70 M. Yusuf, S. Song, S. Park and K. H. Park, *Appl. Catal. A*, 2021, **613**, 118025.

71 N. Guo, Y. Zeng, H. Li, X. Xu and H. Yu, *Mater. Lett.*, 2017, **209**, 417–420.

72 T. Ilyas, F. Raziq, S. Ali, A. Zada, N. Ilyas, R. Shaha, Y. Wang and L. Qiao, *Mater. Des.*, 2021, **204**, 109674.

73 S. Kumari, R. Gusain, A. Kumar, N. Manwar, S. L. Jain and O. P. Khatri, *J. CO_2 Util.*, 2020, **42**, 101345.

74 F. Wang, D. Liu, J. Wen and X. Zheng, *J. Environ. Chem. Eng.*, 2021, **9**(5), 106042.

75 J. Wan, X. Du, E. Liu, Y. Hu, J. Fan and X. Hu, *J. Catal.*, 2017, **345**, 281–294.

76 W. Peng, Y. Chen and X. Li, *J. Hazard. Mater.*, 2016, **309**, 173–179.

77 (*a*) K. Jaiswal, Y. R. Girish, P. Behera and M. De, *ACS Org. Inorg. Au*, 2022, **2**, 205–213; (*b*) Y. R. Girish, R. Biswas and M. De, *Chem.–Eur. J.*, 2018, **24**(52), 13871–13878; (*c*) Y. R Girish, R. Biswas and M. De, *Catal. Sci. Technol.*, 2019, **9**, 1201–1207.

78 H. H. Shin, E. Kang, H. Park, T. Han, C. H. Lee and D. K. Lim, *J. Mater. Chem. A*, 2017, **5**, 24965–24971.

79 P. Xing, P. Chen, Z. Chen, X. Hu, H. Lin, Y. Wu, L. Zhao and Y. He, *ACS Sustainable Chem. Eng.*, 2018, **6**(11), 14866–14879.

80 H. Li, Y. Liu, Y. Liu, L. Wang, R. Tang, P. Deng, Z. Xu, B. Haynes, C. Sun and J. Huang, *Appl. Catal. B*, 2021, **281**, 119476.

81 X. Liu, X. Han, Z. Liang, Y. Xue, Y. Zhou, X. Zhang, H. Cui and J. Tian, *J. Colloid Interface Sci.*, 2022, **605**, 320–329.

82 M. S. Yu, S. C. Jesudass, S. Surendran, J. Y. Kim, U. Sim and M. K. Han, *Appl. Mater. Interfaces*, 2022, **14**(28), 31889.

83 H. Cao, C. Jia, H. Zhang, G. Hou, Y. Tang and G. Zheng, *New J. Chem.*, 2021, **45**, 10608.

84 N. Kumar, S. Kumar, R. Gusain, N. Manyala, S. Eslava and S. S. Ray, *ACS Appl. Energy Mater.*, 2020, **3**(10), 9897–9909.